*Advanced Optical Materials*

ADVANCED OPTICAL MATERIALS
www.advopticalmat.de

RESEARCH ARTICLE OPEN ACCESS

# Nanocrystal Quality–Controlled Scintillation in Porous YAG:Ce Aerogels

Pavlo Mai[1] | Yannis Cheref[1,2] | Raphael Marie-Luce[2] | Frédéric Lerouge[2] | Julien Houel[1] | Gilles Ledoux[1] | Alice Perret[1,3] | Francesca Cova[4] | Mauro Fasoli[4] | Benoit Sabot[3] | Frédéric Chaput[2] | Christophe Dujardin[1,5]

[1]Université Lyon1, CNRS, Institut Lumière Matière, UMR 5306, Villeurbanne, France | [2]Ecole Normale Supérieure de Lyon, CNRS, Université Lyon1, Laboratoire de Chimie, UMR 5182, Lyon, France | [3]Université Paris Saclay, CEA, LIST, Laboratoire National Henri Becquerel, Palaiseau, France | [4]Dipartimento di Scienza dei Materiali, Università degli Studi di Milano-Bicocca, Milan, Italy | [5]Institut Universitaire de France (IUF), Paris, France

**Correspondence:** Benoit Sabot (benoit.sabot@cea.fr) | Frédéric Chaput (chaput@univ-lyon1.fr) | Christophe Dujardin (christophe.dujardin@univ-lyon1.fr)

**Received:** 23 December 2025 | **Revised:** 7 March 2026 | **Accepted:** 31 March 2026

**Keywords:** aerogel | ionizing radiation | nanocrystals | scintillators

## ABSTRACT

The development of porous scintillators is an emerging field for the detection of pure beta emitters in gas, as well as for long-lived, low-power batteries and implantable therapeutic emitting devices. Achieving large-area, efficient, and transparent porous scintillators for these applications requires precise control over nanoscintillator parameters and the architecture of the functional material. Aerogels composed of nanoscintillators currently represent the most promising fabrication route, enabling the production of large, translucent structures. However, while optical transparency favors the smallest nanoparticles, optimal scintillation performance generally requires larger, well-crystallized particles with minimal defects. In this work, we investigate the light yield and scintillation mechanisms of YAG:Ce aerogels as a function of synthesis and post-treatment conditions. Our results show that high-temperature thermal treatment enhances light output under ionizing radiation by a factor of eight, without modifying timing performance. We further demonstrate the extreme sensitivity–and reversibility–of low-temperature atmospheric treatments on the oxidation state of cerium ions. These findings provide new insight into the role of defects in nanoscintillators and open pathways toward the development of more efficient porous scintillator materials.

## 1 | Introduction

Scintillating materials are designed to convert ionizing radiation into optical photons. When coupled with suitable photodetectors and data processing systems, they enable a wide range of applications, including X-ray imaging, radioactivity detection, calorimetry in high-energy physics, rare event searches, and positron emission tomography (PET) [1–5]. The composition of a scintillating material generally determines its light production, which is governed by key scintillation parameters such as light yield, timing, and energy resolution [6]. It also controls the primary interaction efficiency, as illustrated by the need for high material density in high-energy calorimetry or the incorporation of isotopes with high thermal neutron cross-sections when neutron detection is targeted. The shape of the scintillator also plays a crucial role, as it governs the collection efficiency of the emitted light. Depending on the application, scintillators are prepared in various forms: large or small single crystals for high-energy physics or PET, powders as X-ray phosphors for certain imaging applications, layers of needles or thin films for high spatial-resolution imaging [3, 7–11], and bundles of long scintillating fibers for calorimetry [12, 13], which can provide particle discrimination capabilities. They can also be used as nanoparticles, known as nanoscintillators, for applications such as theranostic agents [14–16]. When incorporated into a host matrix, these materials may, in certain cases, emulate the response of bulk

scintillators by generating a well-defined gamma-ray photopeak as illustrated in the following works [17, 18]. Recently, a large-scale BN–perovskite nanocomposite aerogel scintillator, embedding $^{10}$B- as a natural isotope, has demonstrated thermal neutron detection capability together with efficient neutron–gamma discrimination. Here, the aerogel structure maximizes porosity and minimizes density, thereby deliberately suppressing gamma-ray sensitivity [19]. Introducing porosity into scintillating media can also offer significant advantages for specific applications. In particular, it allows the incorporation of the target to be detected directly into the scintillator, which is especially useful when the particle's range is very short. In this context, we recently demonstrated that an ultra-porous YAG:Ce scintillating aerogel can effectively detect the challenging pure beta emitter tritium (H-3, $E_{ave}$ = 5.7 keV) with a detection efficiency of 20%, while krypton-85 (Kr-85, $E_{ave}$ = 251 keV) is detected with an efficiency of 95% [20]. Similarly, scintillating metal–organic frameworks (MOFs), prepared either as powders or single crystals, have been studied with the same objective [21, 22]. Following the same strategy of incorporating the radioactive element into the scintillator, porous scintillators can be advantageous for the long-term generation of light, whether for therapeutic applications such as Parkinson's and Alzheimer' disease treatment [23, 24] or for long-lived, low-power nuclear batteries [25, 26].

In this paper, we focus on the well-known YAG:Ce composition, prepared as nanoparticles and used to form the scintillating porous aerogel. Here, we focus on the relationship between the preparation route, composition, post-thermal treatment (and its atmosphere), and their effects on the scintillation mechanisms and performance. This study aims to optimize the performance of porous scintillators to improve detection efficiency for radioactive gases, including pure beta emitters and radon-222 ($^{222}$Rn).

## 2 | Methods and Preparation

### 2.1 | Synthesis of YAG:Ce Nanoparticle-Based Aerogel Monoliths

Aluminum isopropoxide was purified by distillation. Meanwhile, hydrated yttrium acetate and cerium acetate (both from Sigma–Aldrich Chemie, France) were dehydrated under vacuum. The reagent-grade solvents (1,4-butanediol, diethylene glycol, acetone, diethyl ether, ethanol, and 1,4-dioxane; all from Sigma–Aldrich Chemie, France) were used as received, without further purification.

#### 2.1.1 | Synthesis of Highly Water-Dispersible YAG:Ce Nanoparticles

YAG:Ce nanoparticles were synthesized using a glycothermal method according to the protocol described in our previous work [20, 27]. The experimental procedure for preparing nanoparticles with a stoichiometric composition of $Y_{2.988}Ce_{0.012}Al_5O_{12}$ (0.4 at.% cerium) is detailed below: First, 42.9 g (210 mmol) of distilled aluminum isopropoxide, 33.4 g (125.6 mmol) of dehydrated yttrium acetate, and 0.160 g (0.5 mmol) of dehydrated cerium acetate were suspended in 1,200 g of 1,4-butanediol and 235 g of diethylene glycol. After stirring until completely homogenized, the suspension was transferred to a 3 L autoclave and heated to 300°C for two hours. After cooling, the nanoparticles were purified from the crude product using a two-step process: First, the tetrahydrofuran and acetic acid formed during the reaction were removed by vacuum. Then, the mixture was precipitated and centrifuged using a diethyl ether/acetone mixture. The obtained nanoparticles were dispersed in deionized water to form an aqueous colloid. This was then treated with concentrated HCl to remove surface ligands. After several precipitation-centrifugation steps, the "bare" nanoparticles were resuspended in deionized water. The colloidal solution underwent a dialysis step to remove ionic and organic impurities completely. Finally, the purified colloid was concentrated under vacuum until a solid content corresponding to 40% by weight was obtained for the preparation of gels. The precursor masses were adapted for different cerium concentrations.

#### 2.1.2 | Preparation of Aerogels

Gelation was initiated by the controlled addition of ethanol and 1,4-dioxane to the colloid that had been previously prepared. Different proportions were tested to optimize the conditions for gelation. The results obtained for particles doped with 0.4 at.% Ce (Figure 1-a) demonstrate the following: (i) an excess of 1,4-dioxane leads to either a multiphase system (gel suspended in a liquid; purple dots in Figure 1a) or a monolithic gel containing air bubbles due to overly rapid gelation (blue dots in Figure 1a); (ii) gelation could not be achieved in mixtures with a high colloid content (orange dots in Figure 1a) or gelled only after prolonged exposure to 50°C (orange/green dots in Figure 1a); and (iii) an excess of ethanol prevented gelation. A range of compositions conducive to the formation of homogeneous monolithic gels was identified (green dots in Figure 1a). The 3:5:2 mass ratio (colloid:ethanol:1,4-dioxane) was selected because it allows for rapid gelation within a few tens of minutes. The mixtures were immediately transferred to molds consisting of a glass cylinder closed at both ends by two PTFE discs held in place by metal plates. After 24 h, gelation was complete (Figure 1b). The gels were then aged for 48 h at 40°C in a 1,4-dioxane vapor-saturated atmosphere, resulting in transparent, stable monoliths. To prevent drying or cracking, the gels were immersed in a 1,4-dioxane/acetone mixture. According to a protocol, the interstitial liquid was gradually replaced by acetone in 20% volume increments, with each step lasting at least 12 h. Finally, the acetone was removed via supercritical drying using a Leica supercritical dryer. This process fully preserved the nanoporous microstructure and yielded crack-free monolithic aerogels. The aerogels were heat-treated for one hour between 500 and 1,000°C to improve the crystallinity of the YAG nanoparticles while maintaining the monoliths' maximum transparency in the visible range. These annealing processes were carried out under different atmospheres to control the degree of cerium oxidation. Treating the aerogels in air or a reducing atmosphere ($H_2$/Ar) promotes the 4+ or 3+ oxidation state of cerium, respectively. These treatments were accompanied by a change in color (Figure 1c).

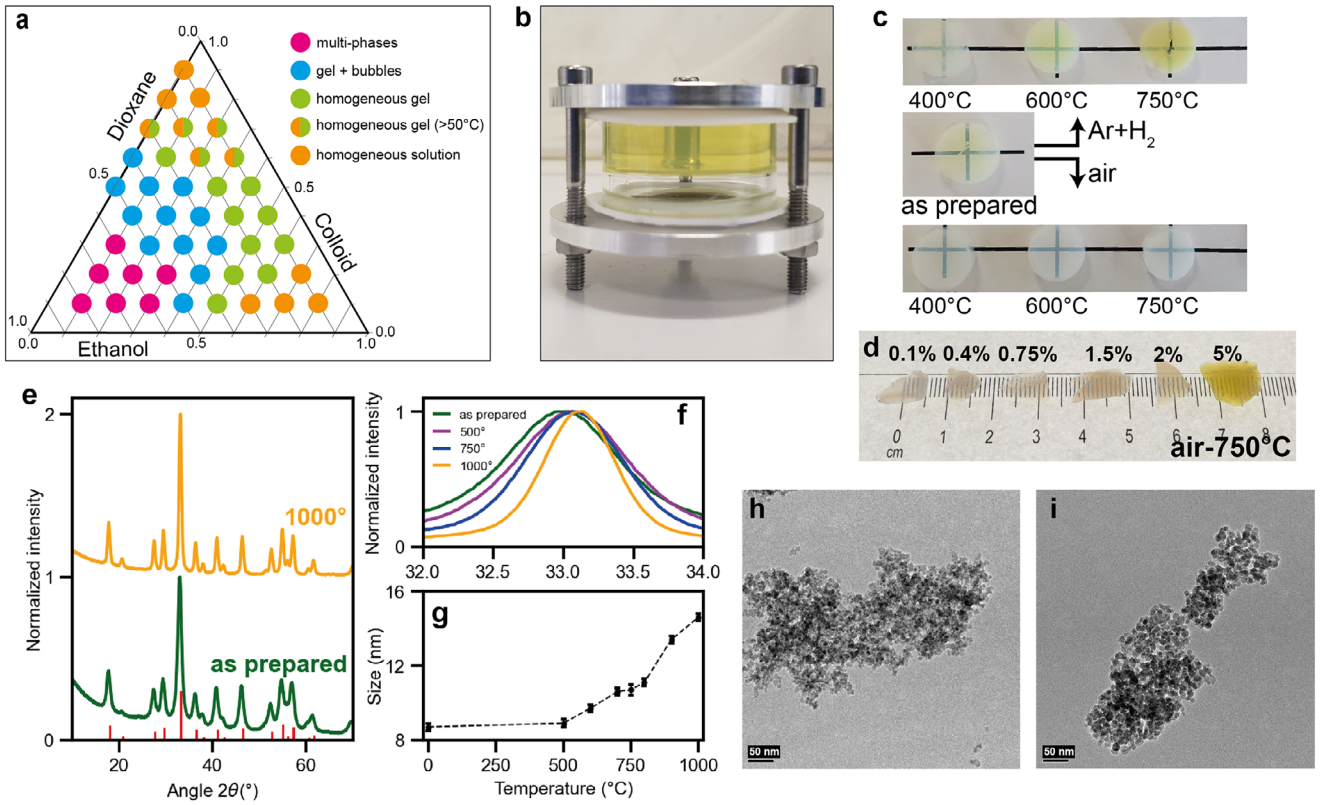


**FIGURE 1** | (a) Mass-based ternary diagram illustrates the range of sample compositions prepared within the colloid/1,4-dioxane/ethanol system. (b) Gel formed by the self-assembly of YAG:Ce nanoparticles within its glass mold. (c) As-prepared YAG:Ce (0.4 at.%) aerogel and the corresponding aerogels after various thermal treatments in air and in an $Ar/H_2$ atmosphere. (d) Fragments of aerogels doped with various cerium concentrations and treated in air at 750°C. (e) XRD patterns of 0.4 at.% Ce-doped YAG nanoparticles forming the aerogels, shown as-prepared and after thermal treatment at 1000°C in air. The most intense diffraction peaks were identified according to the ICDD card (# 00-033-0040) shown as the red bar plot. (f) Evolution of the (420) peak as a function of thermal treatment. (g) Nanoparticle size evolution, determined by Scherrer analysis, as a function of the aerogel thermal treatment temperature.Transmission electron microscope images of the nanoparticles in the as-prepared aerogel (h) and after thermal treatment at 750°C (i).

The yellow color characteristic of $Ce^{3+}$disappears after annealing in air, but remains in a reducing atmosphere. In both cases, the aerogels shrink, become less transparent, and grow more mechanically resistant as the annealing temperature increases, particularly above 750°C. Aerogels with varying cerium doping levels were developed using the same experimental protocol. For doping levels greater than or equal to 1.5%, the aerogels exhibited persistent yellow coloring even after annealing in an oxidizing atmosphere. This phenomenon indicated incomplete conversion of $Ce^{3+}$ions to $Ce^{4+}$, suggesting limited oxidation kinetics under these conditions (Figure 1d).

#### 2.1.3 | Structural Characterizations

We characterized crushed aerogel fragments using X-ray diffraction. Only diffraction peaks characteristic of the YAG phase were detected for all samples (Figure 1e), confirming the absence of unwanted phases. After annealing, noticeable refinement of the peaks was observed (Figure 1f), reflecting improved crystalline order. Analysis of the peak width, performed on fragments annealed in air between 500 and 1000°C using the Scherrer method, revealed a gradual increase in nanocrystal size (Figure 1g). This increase was directly correlated with the growing diffusivity of the aerogels. This microstructural evolution was confirmed by transmission electron microscopy (Figure 1h,i).

### 2.2 | Optical and Scintillation Spectroscopies

Optical absorption, photoluminescence (PL), and photoluminescence excitation (PLE) spectroscopies of the colloidal solution of YAG:Ce nanoparticles (NPs) were performed using an FS5 spectrofluorimeter (Edinburgh Instruments). Fluorescence Quantum yields (QYs) were extracted from measurement with an integration sphere: module SC-30 coupled to FS5 spectrofluorometer from Edinburgh Instruments. Samples were excited at $\lambda = 450$ nm. A reference measurement was taken at the same excitation wavelength, with no sample in the integrating sphere. The analysis of the spectra from 400 to 700 nm, i.e., including the excitation wavelength, allows the absorption and emission intensities to be estimated, and the quantum yield to be determined using the software *Fluoracle*. Absorption spectra of aerogel fragments were measured with a Lambda 950 UV/VIS double-beam spectrometer (PerkinElmer) equipped with a Spectralon-coated integrating sphere to collect scattered light.

Radioluminescence (RL) spectra were measured with a miniX2 X-ray source from Ametek, equipped with a tungsten anode (ref. MNX2-911-W), operated at 50 kV and 200 μ A, as the excitation source. No X-ray filters were used. The emitted light was collected using a UV optical fiber coupled to a Shamrock SR-500i-D2 imaging spectrograph (Andor). A 149 lines/mm grating, blazed at 300 nm, was used for spectral dispersion. The system was equipped with a Newton EMCCD detector (Andor).

Luminescence decay times were measured using two different excitation sources. For 450 nm excitation, a pulsed diode DeltaDiode-440L from Horiba, emitting at 440 nm +/- 10 nm was used. The excitation beam was spectrally cleaned with a bandpass optical filter centered at 440 nm. For X-ray excitation, a pulsed diode DeltaDiode-405L from Horiba, emitting at 405 nm, was used to illuminate the photocathode of an X-ray tube (model N5084, Hamamatsu) operated at 35 kV. In both cases, the excitation repetition rate was set to 100 kHz. The emitted light was collected through a longpass filter at 500 nm. Detection was performed using a PMA-C photomultiplier tube (PicoQuant). Time-resolved measurements were carried out using a PicoHarp 300 time-correlated single-photon counting system (PicoQuant), with a time bin of 512 ps per channel. Each decay curve was recorded over a time window of 4 μ s.

The Triple-to-Double Coincidence Ratio (TDCR) method was a widely used approach in metrology for evaluating the scintillation yield of a scintillating medium. This technique was based on a triple-coincidence detection system and, assuming a Poissonian distribution of emitted photons, the ratio of triple to double coincidences was directly related to the mean number of detected photons per event [28]. While TDCR was traditionally applied to liquid scintillators, it had recently been extended to both organic and inorganic scintillators, with the additional capability of energy selection, as demonstrated in Compton-TDCR experiments [29].

Low temperature RL, X-ray irradiation resistance and afterglow measurements were performed by exciting the samples by unfiltered X-ray irradiation using a Philips PW2274 X-ray tube, equipped with a tungsten target and a beryllium window and operated at 20 kV. At this operating voltage, X-rays were produced by the Bremsstrahlung mechanism superimposed to the L and M transition lines of tungsten due to the impact of electrons generated through a thermionic effect and accelerated onto the tungsten target. A dose rate of 5.5 $mGy.s^{-1}$, evaluated with a calibrated ionization chamber in air, was used. The radioluminescence was collected using a custom apparatus featuring a liquid nitrogen-cooled, back-illuminated, and UV-enhanced CCD detector (Jobin-Yvon Symphony II) coupled to a monochromator (Jobin-Yvon Triax 180) with a 100 lines/mm grating. RL measurements were performed in the 10–320 K interval by lowering the temperature with a closed-cycle He cryostat and controlling the temperature with a Lakeshore 330 temperature controller.

Thermally stimulated luminescence. Wavelength-resolved TSL measurements below room temperature were carried out using the same detection system as for RL measurements. TSL measurements were performed in the 10–320 K interval, with a heating rate of 0.1 $K.s^{-1}$ after X-ray irradiation up to 4.6 Gy. A typical TSL measurement consists in a preliminary X-ray irradiation at low temperature (T = 10 K in our case) to fill trap states in the bandgap that were stable at the chosen temperature: successively, the irradiation was ceased, and the temperature was progressively raised with a constant heating rate while monitoring the delayed emission due to carrier de-trapping. The shape of the TSL signal versus T (the so-called glow curve) had been corrected for the variation of the RL emission intensity versus T, to decouple the trap contribution to the emission from the other mechanisms involved in the scintillation process.

## 3 | Results and Discussion

### 3.1 | Optical Spectroscopies

The colloidal solution containing the as-prepared YAG:Ce nanoparticles appears yellow, indicating that a significant fraction of cerium is in the trivalent state. Under blue excitation at 440 nm, it exhibits the well-known broad yellow emission peaking at about 550 nm, characteristic of the 5d–4f transition (Figure 2a). The corresponding excitation spectrum also shows the characteristic excitation bands (340 and 450 nm) associated with the 4f–$5d_1$ and 4f–$5d_2$ transitions of $Ce^{3+}$. An additional bump peaking at approximately 417 nm is observed (Fit with three Gaussian functions peaking at 2.73, 2.97, and 3.66 eV is provided in Figure S1). This extra band at 2.97 eV has also been reported in YAG:Ce nanoparticles [30–32]. This may be attributed to cerium ions located at the surface of the as-prepared nanoparticles, which exhibit structural disorder and experience a different crystal field. When measuring the absorption spectrum of the solution, only the first band at 450 nm can be distinguished. Additional strong absorptions and diffusion, mask the weaker 4f–5d absorption bands. For aerogel thermally treated at 750°C, the PL spectrum under excitation at 440 nm is also characteristic of YAG:$Ce^{3+}$. Across all thermal treatment temperatures, the PL spectra remain very similar (Figure 2b. The PLE spectrum of the as-prepared aerogel sample, presented in Figure 2b, is, as expected, very similar to that observed for the same nanoparticles in solution, which were used to form the aerogel. At 1000°C, the excitation spectrum closely resembles that typically observed in single crystals. Such thermal treatment induces a structural rearrangement of the nanocrystals, supporting the hypothesis that the additional excitation band around 400 nm in the as-prepared samples originates from perturbed surface disorder, likely located near the nanocrystal surface. We then measured the PL spectra under 420 and 430 nm excitation, where this unusual band overlaps with the regular excitation band (Figure S2a,b). With increasing thermal treatment temperature under an $Ar/H_2$ atmosphere, the amplitude of the blue-shifted emission decreases, while the regular emission intensity increases. These results indicate that thermal treatment promotes, as expected, the rearrangement of the crystalline structure, leading to an optical response that progressively approaches that of bulk single crystals. The absorption spectrum clearly shows the band at 450 nm, whereas the UV band is masked by optical scattering from the sample. When the sample is treated in an air atmosphere, the absorption band at 440 nm disappears, indicating the oxidation of $Ce^{3+}$to $Ce^{4+}$(Figure 2b. The resulting sample loses its yellowish color (Figure 1c). Finally, the RL spectrum of the aerogel treated in $H_2$ is very similar to its spectrum (Figure 2b).

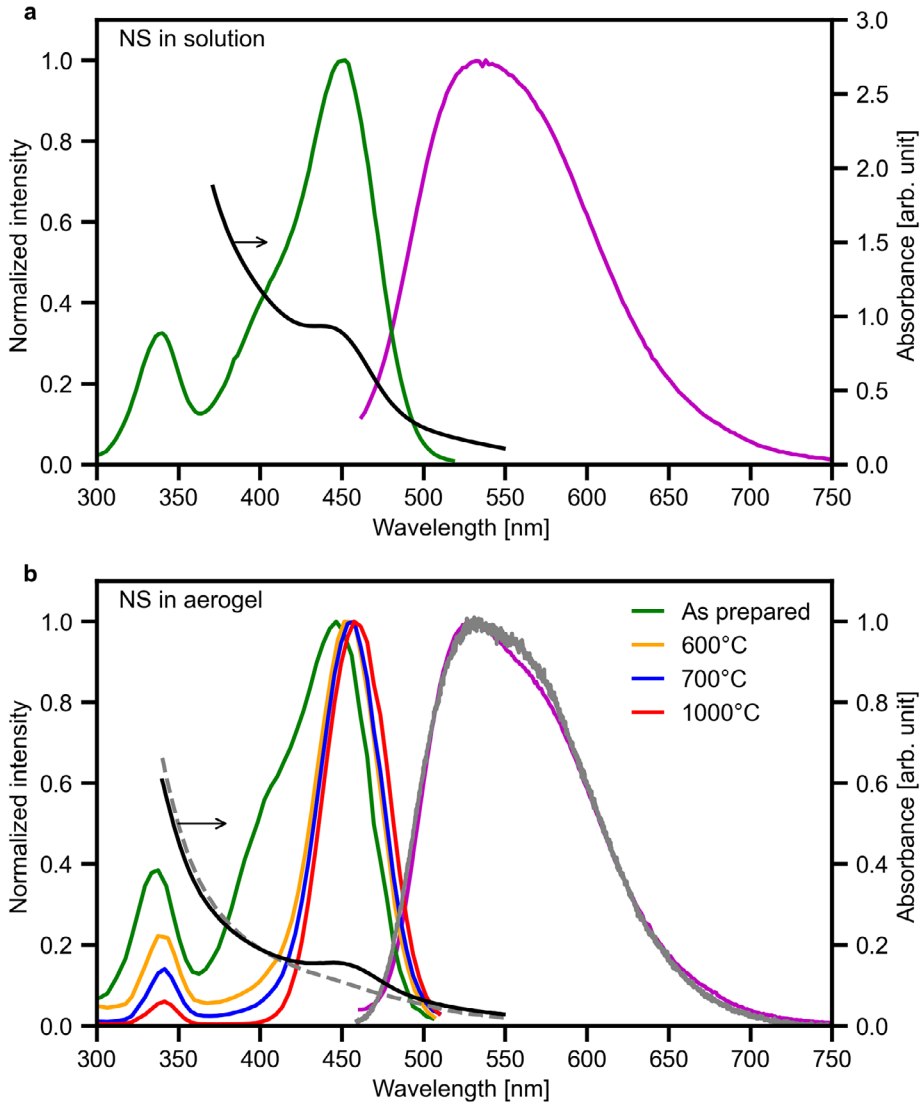


**FIGURE 2** | (a) Optical PL (purple) (excitation at 440 nm), PLE (green) (emission at 550 nm), and absorption (black) spectra of YAG:Ce nanocrystals in colloidal solution. (b) Room-temperature photoluminescence (PL, purple, excitation 450 nm) and radioluminescence (RL, solid grey) spectra of YAG:Ce aerogels after thermal treatment in $H_2$ at 750°C. Photoluminescence excitation (PLE, emission 550 nm) spectra of YAG:Ce aerogels for various annealing temperatures: green = as-prepared, yellow = 600°C, blue = 700°C, and red = 1000°C. Absorbance spectra of YAG:Ce aerogels after thermal treatment in $H_2$ (black) and in air (grey, dashed) at 750°C.

### 3.2 | Cerium Concentration and Oxidation State

As discussed in the sample preparation section, thermal treatment influences both the shrinkage and the transparency of the resulting aerogel. It is also well established that the scintillation yield and timing performance depend on the cerium concentration. Furthermore, unlike PL, where cerium must be in the $Ce^{3+}$ state to be optically active, the scintillation process under ionizing radiation can also involve $Ce^{4+}$. In this case, sequential hole and electron trapping by cerium ions enables $Ce^{4+}$ to participate in the scintillation mechanism. The presence of $Ce^{4+}$ is even beneficial, as it accelerates the time response and enhances the scintillation yield in situations where competition with charge trapping occurs. This mechanism has been extensively studied in various systems, such as $Lu_2SiO_5$ [33], several garnet single crystals [34], silica [35], and reviewed in [2, 3].

In our previous study on the real-time detection of beta emitters in gas, we prepared large samples with a cerium concentration of 0.4%, thermally treated in air at 750°C[20]. This choice was based on powder optimization and on the transparency of the large pieces, which directly affects light collection. In the present work, we investigate in detail the optical and scintillation properties of samples with Ce concentrations ranging from 0.1% to 5%, and aerogels thermally treated between 500 and 1000°C. In addition, we compare the influence of cerium valency by considering thermal treatments in air (white samples, predominantly $Ce^{4+}$) and in reducing Ar+$H_2$ mixture atmosphere (yellowish samples, predominantly $Ce^{3+}$) (Figure 1c). The study is carried out on small fragments, thus minimizing the effect of transparency variations. We first discuss the influence of cerium concentration in aerogels treated at 750°C, followed by an investigation of the thermal treatment effect on the 0.4% Ce sample.

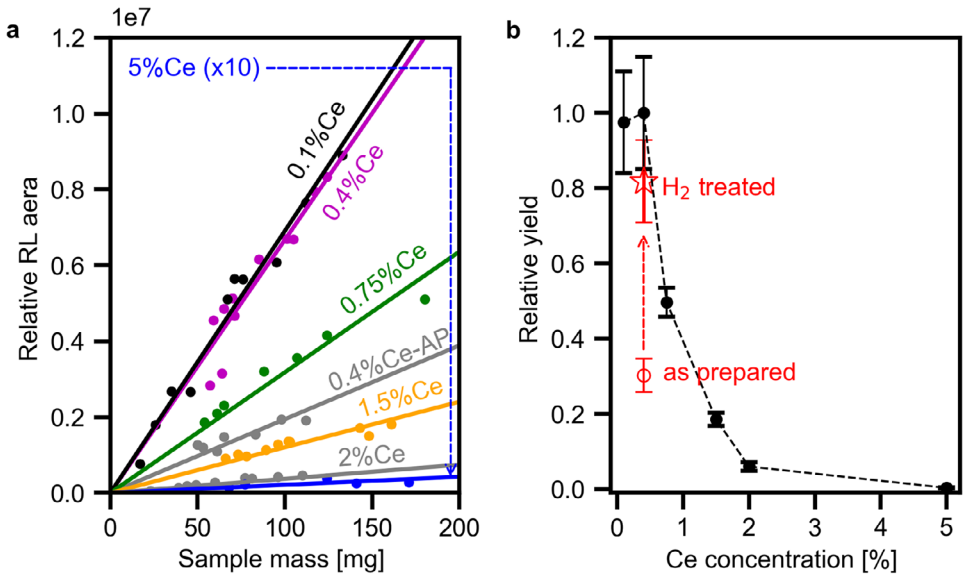


**FIGURE 3** | (a) Evolution of RL intensity as a function of sample mass for different cerium concentrations in aerogels treated at 750°C under air. The solid lines correspond to linear fits of the experimental data for each cerium concentration. (b) Relative yield, deduced from (a) as a function of cerium content. Error bars represent the standard deviation of LY/mass for each measurement set. The 0.4% Ce sample as-prepared (open circle) and after $H_2$ treatment (open star) are also shown.

The measurement of the relative scintillation yield of aerogels is a complex process. The amount of detected light depends both on the mechanisms of light production and on its subsequent collection. The latter is influenced by the optical quality and the configuration of the sample. For a given composition, X-ray absorption scales linearly with sample mass in the weak-absorption limit. We then designed a protocol that can be referred to as the "multi-sample mass" method. The current manufacturing capacity is sufficient to produce large pieces; however, the final shape exhibits variability. Due to the fragility of the samples, cracking has been observed. This issue was mitigated by deliberately dismantling the object into multiple components, as pieces illustrated in Figure 1i. For each composition and geometry, a set of 6–10 samples was carefully weighed and placed in polyethylene liquid scintillation vials (see Revvity, PICO PRIAS VIAL). During radioluminescence spectral acquisition, the vial was mounted on a rotating stage to average the collected light across the sample. An illustrative series of RL spectra for different YAG:0.1%Ce samples is shown in Figure S3. In the weak absorption regime, the absorption varies linearly with the sample mass. As expected, when the RL area is plotted as a function of the sample mass, a linear behavior is observed. As shown in Figure 3a, A similar behavior, but with different slopes, is observed for various cerium concentrations. Both the fitting procedure and the average intensity-per-mass value yield consistent results. Throughout the discussion, we report the latter, with error bars representing the standard deviation.

The plot presented in Figure 3b shows the evolution of the relative scintillation yield at room temperature for aerogels treated at 750°C in air (i.e., $Ce^{4+}$), with various cerium concentrations ranging from 0.1% to 5%. The plot is normalized to its maximum, which occurs for the sample containing 0.4% of Ce. A typical behavior is observed, with the scintillation yield decreasing for cerium concentrations above 0.4%, reflecting the well-known phenomenon of concentration quenching, as well as possible $Ce^*$–$Ce^*$ Auger quenching occurring under X-ray excitation. Remarkably, using this measurement technique, we observe that the scintillation yield of the Ar+$H_2$-treated sample (i.e., for $Ce^{3+}$) is approximately 20% lower than that of the air-treated analog. For the same cerium concentration, the as-prepared sample exhibits a scintillation yield that is approximately 30% of that of the thermally treated sample. This result indicates that, beyond mechanical reinforcement, thermal treatment plays a role in the crystallization state, which most likely heals the material from non-radiative defects.

450 nm and X-ray-excited decay time measurements were recorded on the same series of samples and are presented in Figure 4a,b, as well as Figure S4. To enable consistent comparison across all measurements, the decay curves were fitted using a multi-exponential model, with the number of components left unconstrained. Details of this Laplace fitting procedure are provided in the (Figures S5 and S6). From these fits, effective lifetimes ($\tau_{eff}$), weighted by their amplitudes, were extracted (Table 1). This method avoids the need to predefine the number of components, which is particularly uncertain in cases of strongly non-exponential behavior. The evolution of $\tau_{eff}$ as a function of cerium concentration is presented in Figure 4c.

When excited directly at 450 nm, the aerogel with the lowest cerium concentration (0.1% Ce) is outside the range where concentration quenching is expected to occur. Bachmann et al. [36] have measured the decay time for a series of YAG:Ce powders and found a single-component decay time of about 65 ns for the lowest Ce concentration. For higher Ce concentrations, they observed an increase in the measured decay time, which they attributed to a potential self-absorption re-emission sequence. High concentrations of cerium have also been achieved using a solvothermal synthesis route by Cantarano et al. [37] They reported decay times ranging from approximatively 120 ns for a 0.5%-doped sample to 15 ns for an 8%-doped sample. These

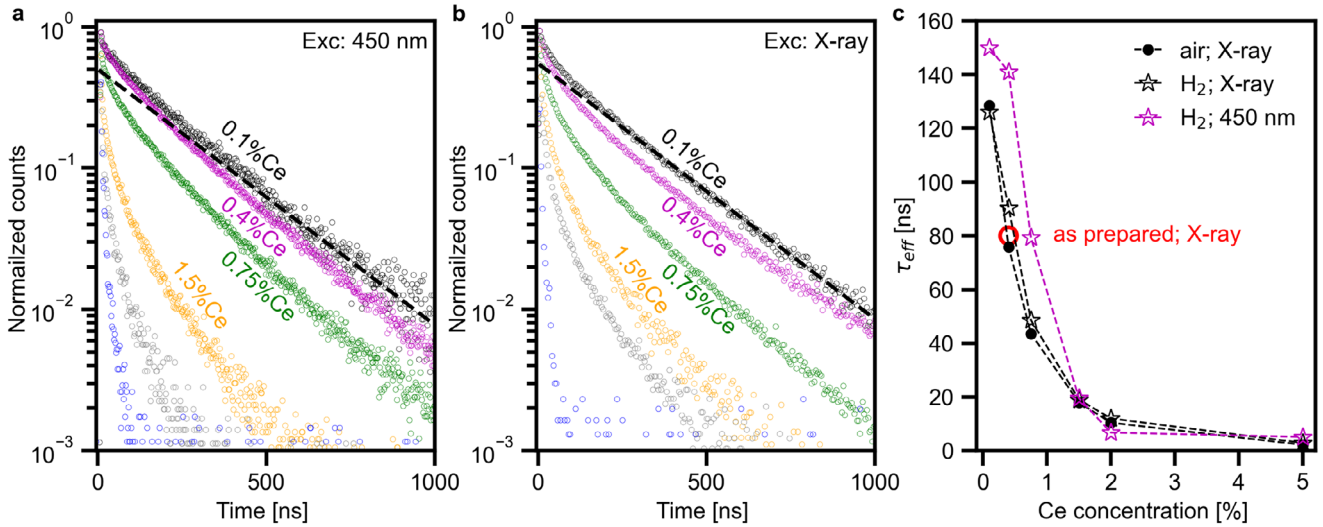


**FIGURE 4** | (a) Decay under 450 nm excitation of aerogels treated at 750°C under Ar+$H_2$ mixture for various cerium concentrations. (b) Decay under X-ray excitation of aerogels treated at 750°C under Ar+$H_2$ mixture for various cerium concentrations. To guide the eye, the dashed black line corresponds to a single-exponential component with a decay time of 240 ns. (c) Effective decay time as a function of cerium concentration under X-ray excitation for air-treated (solid black circles) and Ar/$H_2$-treated samples (open stars), and for the Ar/$H_2$-treated sample under 450 nm excitation (open purple stars). The open red circle corresponds to the effective decay time of the as-prepared aerogel doped with 0.4% Ce under X-ray excitation.

**TABLE 1** | Amplitude-weighted effective decay time ($\tau_{eff}$), deduced from the Laplace fitting procedure, for YAG:Ce aerogels thermally treated at 750°C in air and in Ar/$H_2$ at various cerium concentrations.

| Ce content at.% | 450 nm; Ar/$H_2$ $\tau_{eff}$ (ns) | X-ray; Ar/$H_2$ $\tau_{eff}$ (ns) | X-ray; air $\tau_{eff}$ (ns) |
|---|---|---|---|
| 0.1 | 149.9 | 126.1 | 128.4 |
| 0.4 | 141.1 | 90.4 | 75.9 |
| 0.75 | 79.3 | 48.6 | 43.6 |
| 1.5 | 19.5 | 19.0 | 17.9 |
| 2 | 6.7 | 12.0 | 10.4 |
| 5 | 5.1 | 2.9 | 2.2 |

measurements were performed on agglomerated nanoparticles (30–40 nm in diameter) in powder form. In our measurements, a slight initial quenching is observed, which we attribute to emission from cerium ions located in imperfect environments, such as near the surface of the nanoparticles. In the case of our relatively small nanoparticles (around 10 nm in diameter), this effect is particularly pronounced due to the high surface-to-volume ratio. The dashed black line indicates the radiative decay time of the non-quenched centre, which is approximately 240 ns. We remark then the strong dispersion in the decay time measurements, ranging from 65 ns for micrometric powders to 240 ns for highly nanoporous aerogels, with a value of about 120 ns for agglomerated nanoparticles. We attribute these pronounced differences to the influence of the effective refractive index on the radiative decay time. In nanostructured materials, the effective refractive index experienced by an emitter depends on the local optical environment, which must be averaged over distances on the order of 200 nm. [38, 39] This effect has been reported in several systems, including $Y_2O_3$:Eu, YAG, and LuAG:Ce. [40–42]

Following the analysis presented in [40], the volume fraction $x$ of the active material with refractive index $n_{mat}$ embedded in a medium of refractive index $n_{med}$ can be used to estimate the effective refractive index as: $n_{eff} = x.n_{mat} + (1-x).n_{med}$. For this purpose, we consider the model proposed by Meltzer et al., which assumes that the radiative lifetime is proportional to the effective refractive index according to $\frac{1}{n}(\frac{1}{3}(n^2+2))^{-2}$. Considering the refractive index of bulk YAG ($n_{mat} = 1.83$) and that of air ($n_{med}$=1), a composite material consisting of approximately 28% YAG and 72% air would yield an effective refractive index consistent with a change in the radiative decay time from 65 to 240 ns. This value agrees remarkably well with the porosity of about 33% determined from BET measurements [20].

A clear shortening of the decay time is observed when the cerium content increases for both 450 nm and X-ray excitation. This effect is already remarkable, as such a reduction in decay time has not been observed in polycrystalline Ce-doped YAG with doping levels up to 3%. At room temperature, the decay time is consistently reported to be around 60–65 ns. Lin et al. observed at room temperature a slight decrease in the decay time, from 68 to 60 ns, as the cerium concentration increased from 0.2% to 3% [43]. According to their interpretation, at low temperatures all decay times are expected to be identical, while at room temperature the thermal ionization process leads to an apparent increase in the decay time for weakly doped samples. This variation is attributed to the change in ionization energy with increasing cerium concentration. Since the present measurements were performed at room temperature, we can rule out thermally activated 5d–4f crossover relaxation via electron–phonon coupling and the thermal ionization quenching effect is expected to be significantly weaker than what we observe. The dominant mechanism is thus identified as concentration quenching, resulting from nonradiative energy transfer among $Ce^{3+}$ ions toward luminescence killer centers. The key distinction between nanocrystals and larger crystals is their higher

density of surface-related nonradiative traps, which accounts for the observed differences in concentration quenching. The fluorescence decay times under optical and X-ray excitation exhibit the same general trend (Figure 3b), though with notable differences. At low cerium concentrations, the effective decay time under optical excitation is slightly longer than under X-ray excitation. This effect does not imply that the intrinsic radiative decay time changes between 450 nm excitation and X-rays, since there is no reason for such a variation in an activated insulator. This interpretation is supported by the slower component of the decay, which follows the same slope as the dashed line corresponding to a single-exponential component with $\tau = 240$ ns. This discrepancy may reflect fundamental differences in the excitation mechanisms. Under optical excitation, all absorbing and emitting $Ce^{3+}$ions contribute directly to the decay. In the case of ionizing radiation, however, cerium excitation proceeds through intermediate states–namely free electrons and holes–so that a competition arises between capture by the active centers and trapping at defect states. This effect is particularly important in nanoparticles, which generally contain a larger number of structural defects compared to bulk crystals. This indicates that the distribution of excited cerium-ion populations under X-ray excitation differs from that obtained under direct 450 nm excitation. More surprisingly, the as-prepared sample doped with 0.4% cerium exhibits an effective decay time under X-ray excitation almost similar to that of its analogs thermally treated at 750°C in air or in an Ar + $H_2$ mixture. A convincing comparison of these decay time measurements is provided in the (Figure S7). This observation may seem at odds with the scintillation yield analysis, as the as-prepared sample showed a lower yield than the thermally treated one (Figure 3a,b). This suggests that the low scintillation yield in the as-prepared sample arises not from cerium quenching, but rather from electron–hole trapping prior to carrier transfer to the activator.

### 3.3 | Thermal Treatment Effect

Based on the previous section results observed between the as-prepared and thermally treated samples, we investigated the effect of thermal treatment in the temperature range of 500–1000°C on the 0.4% Ce-doped aerogel. Using the above-mentioned 'multi-sample mass' method, we obtained a series of RL intensity evolutions as a function of sample mass for the as-prepared aerogel and samples subjected to thermal treatments in air up to 1000°C. Representative evolutions for selected temperatures are presented in Figure 5a. One may note that the behavior still follows a linear trend, confirming the suitability of the method.

The optical quantum yield was estimated from aerogel fragments, yielding values of 7, 7.4, 13, 23.7, and 33.3% for the as-prepared sample and for samples thermally treated under a reducing atmosphere at 600, 800, 900, and 1000°C, respectively. These measurements should be considered with significant uncertainty due to the uncontrolled shape of the fragments, combined with variations in diffusivity arising from the different thermal treatments. Nevertheless, they reveal a clear overall trend. To investigate the effect of thermal treatment on the scintillation mechanisms, we also measured the luminescence decay time under 450 nm and X-ray excitation. Representative decay curves under both excitations are presented in Figure 5b,c for sample thermally treated in reducing atmosphere. To guide the eye, we also plotted the single-exponential decay corresponding to a 240 ns time constant, as shown in Figure 4b,c. This curve represents the decay in the absence of any quenching effects, neither from the $Ce^{3+}$emitting centers directly excited nor from the scintillation mechanisms themselves. Under 450 nm excitation, the evolution of the fluorescence decay shape as a function of the thermal treatment temperature can be described by a sharp, short component and a slow, slightly non-exponential component. The main difference between the decays is the amplitude ratio of these two dominant components. Considering the area under the dashed blue curve (denoted as $A_{ref}$) as the amount of emitted light in the absence of any quenching, we can extract the relative yield evolution as a function of the thermal treatment temperature by taking the area under the normalized decay divided by $A_{ref}$. The corresponding curve is plotted in Figure 5d (open purple circle). In contrast, the X-ray-induced decay curves are similar for all thermal treatment temperatures (Figure 5c). The corresponding evolution of the estimated yield under X-ray, using the same method, appears flat (Figure 5d). Similar to the previous section, when comparing the as-prepared sample with the sample treated at 750°C, these results appear contradictory. Similar behavior has recently been observed in $YPO_4$:$Ce^{3+}$ nanoparticles [44].

The evolution of the area under the X-ray-induced decay curve shows almost no dependence on the thermal treatment temperature up to 1000°C. It should be recalled that measuring a decay time corresponds to monitoring the evolution of the excited-state population of the emitting centers. In this sense, the method based on decay-time measurements does not account for losses occurring prior to energy transfer to the emitter. This confirms the hypothesis that the increase in scintillation yield with higher thermal treatment temperatures is mainly due to the improved crystallization state, which leads to a reduction in trap density. The similarity of the decays under X-ray excitation, regardless of the thermal-treatment temperature, suggests that the only cerium ions contributing to the X-ray–induced emission are those located sufficiently far from quenching centers. For cerium ions situated near quenching centers, the generated electron–hole pairs are trapped at these centers, preventing these ions from contributing to the excited cerium population and therefore to the decay signal. This situation differs markedly from direct 450 nm excitation, under which all cerium ions are excited.

In Figure 5d, the orange stars indicate a strong dependence of the scintillation yield measured via the multi-sample mass method. To confirm the significant improvement in scintillation yield without any change in timing characteristics, we analyzed a series of thermally treated aerogels using the triple-to-double coincidence method while exposing them to a $^{241}$Am radioactive source [29]. In the present work, this technique was applied to small aerogel samples with masses ranging from 50 to 150 mg. Due to the small size and very low density of the samples, energy selection was not implemented because of insufficient statistics. Consequently, the triple-to-double coincidence ratio includes all events arising from the interaction of the 60 keV gamma photons with the aerogel, resulting in a broad range of electron energies. Unlike multi-mass sample methods, this approach is expected to be much less sensitive to sample mass, since a measurement is registered only when an interaction with a 60 keV gamma photon

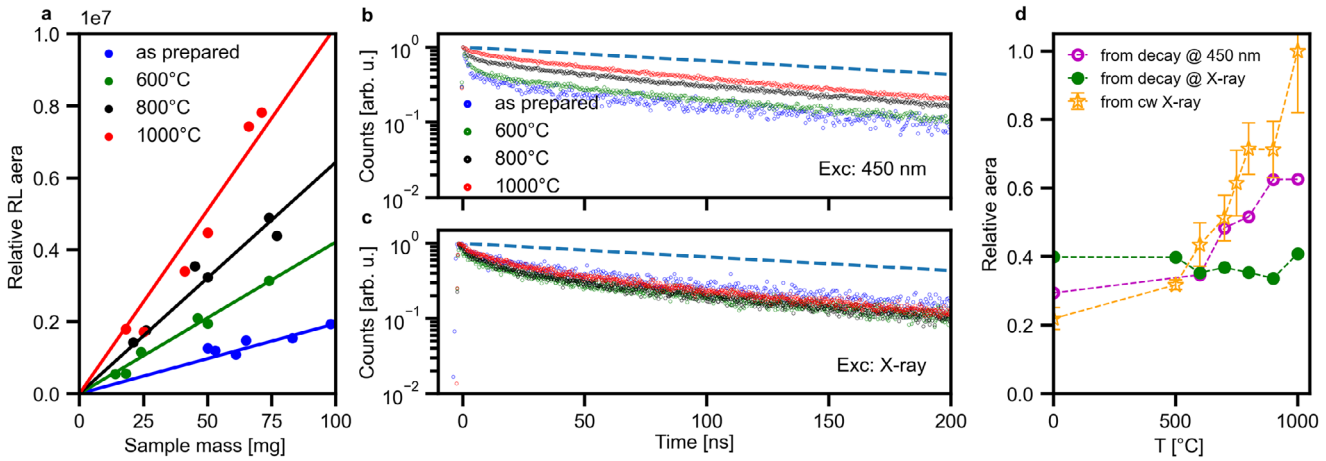


**FIGURE 5** | (a) Evolution of RL intensity as a function of sample mass for different temperatures of thermal treatment in air. The solid lines correspond to linear fits of the experimental data for each cerium concentration. (b) Luminescence decay under 450 nm excitation for YAG:Ce aerogels doped with 0.4% Ce after various thermal treatments in reducing atmosphere. The dashed blue curve corresponds to a single-exponential decay with a lifetime of 220 ns. (c) Luminescence decay under X-ray excitation for YAG:Ce aerogels doped with 0.4% Ce after various thermal treatments in reducing atmosphere. (d) Evolution of the area ratio (measured luminescence decay area divided by the area of the 240 ns single-exponential decay) as a function of thermal treatment temperature for aerogels doped with 0.4% Ce under 450 nm excitation (solid green circles) and X-ray excitation (open purple circles). Open orange stars correspond to the relative scintillation yield under continuous X-ray excitation, obtained using the "multi-sample mass" method.

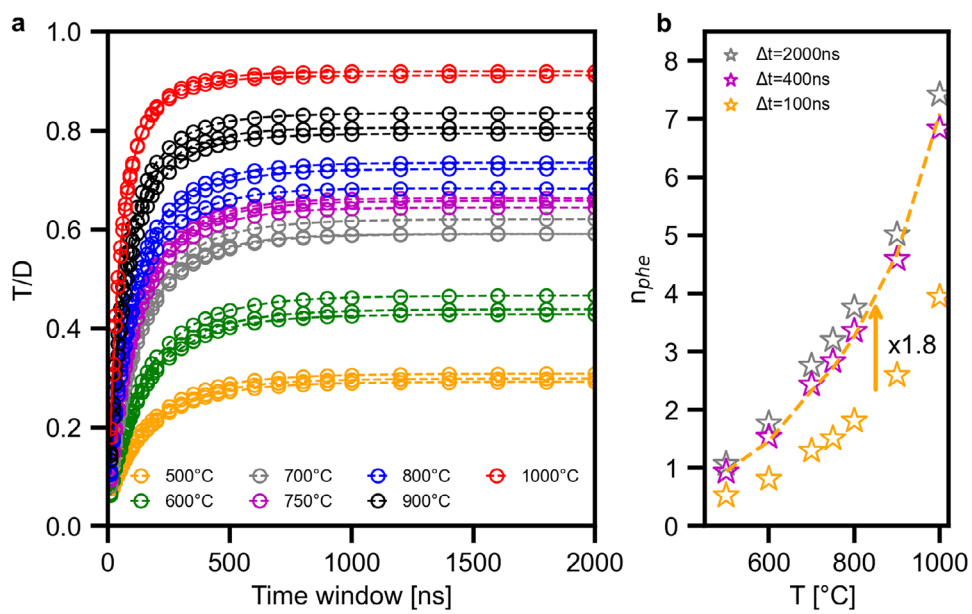


**FIGURE 6** | (a) Evolution of the triple-to-double coincidence ratio (T/D) as a function of the time coincidence window for fragments of YAG:Ce aerogels after thermal treatment for 1 h in air at various temperatures. (b) Deduced mean number of photoelectrons per event for three typical coincidence time windows as a function of the thermal treatment temperature. The yellow dashed line corresponds to the curve obtained for $\Delta t = 100$ ns and is scaled by a factor of 1.8 to compare its shape with that obtained for $\Delta t = 400$ ns.

occurs. It has been demonstrated that the T/D ratio is directly related to the mean number of detected photoelectrons ($n_{phe} = -3log(1 - T/D)$) [28]. The T/D information is therefore directly related to the mean number of photons emitted per event. The only possible mass-related effect arises from the partial escape of energy carried by primary and secondary electrons, which affects the effective mean energy deposited in the aerogel. In Figure 6a, the evolution of the T/D ratio as a function of the coincidence time window is shown. Good reproducibility of the method is observed within this range of sample masses. We further emphasize that the probability of detecting two (or three) photons within a given time window depends both on the mean number of photons emitted per event and on their temporal distribution following the radioactive interaction, i.e., the scintillation decay time. [20] As anticipated from the scintillation decay time measurements, the T/D ratio increases within the first 500 ns and then gradually

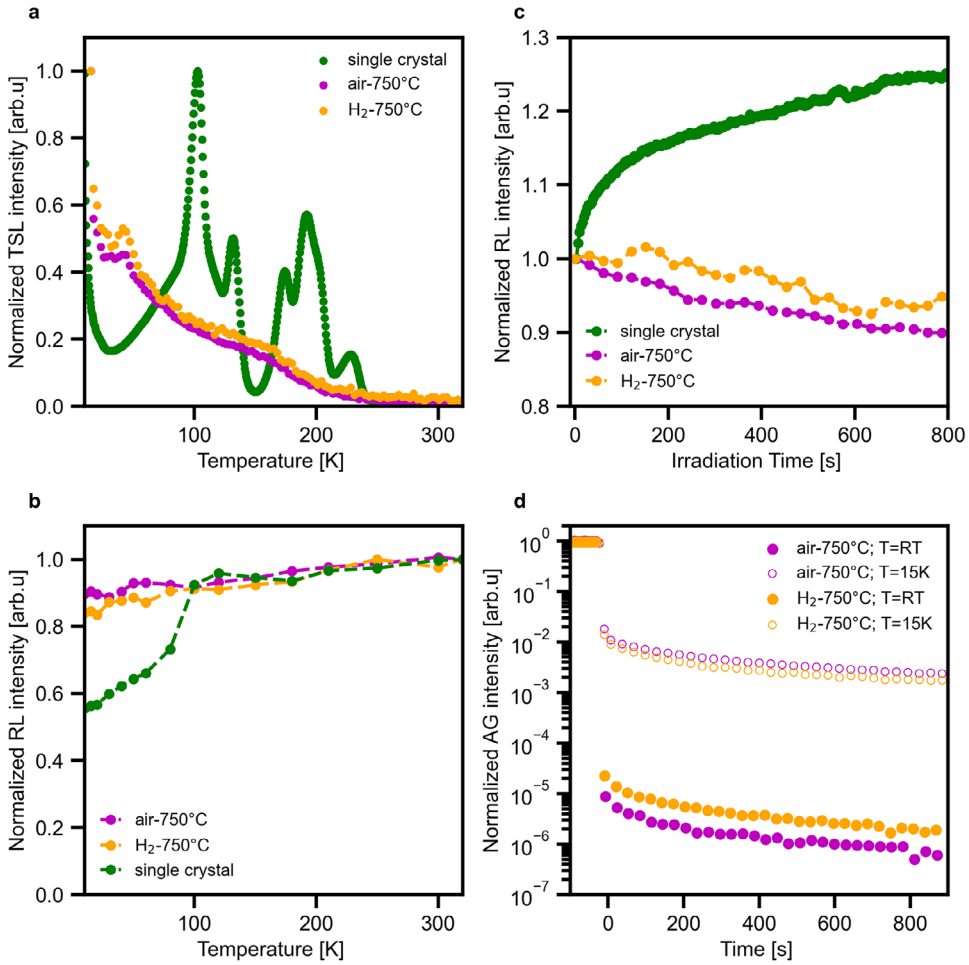


**FIGURE 7** | (a) Thermoluminescence curves showing the response of a reference single crystal and aerogels thermally treated at 750°C under $H_2$ and air atmospheres. (b) Comparison of the temperature dependence of the radioluminescence intensity for a reference single crystal and aerogels thermally treated at 750°°C under $H_2$ and air atmospheres. (c) Dependence of the radioluminescence intensity on irradiation time at T = 20 K for for a reference single crystal and aerogels thermally treated at 750°°C under $H_2$ and air atmospheres. (d) Afterglow decay curves of the two aerogels measured at room temperature and at T = 15 K.

approaches an asymptotic value for longer coincidence time windows. From these data, we can also deduce the evolution of the mean number of detected photoelectrons for various coincidence time windows (namely 100, 400, and 2000 ns, Figure 6b). First, we confirm the significant increase in scintillation yield induced by high-temperature thermal treatments. Second, we observe that a 400 ns coincidence time window is sufficient to collect almost all emitted photons compared with the 2000 ns window (for a detector, shorter time windows also help to reduce fortuitous coincidences). Finally, we compare the evolution of the scintillation yield obtained with a 100 ns time window to that obtained with a 400 ns window. After scaling the 100 ns curve by a factor of 1.8, no significant difference in shape is observed, confirming that the scintillation decay time remains unchanged upon thermal treatment (Figure 6b).

### 3.4 | Role of Traps

We have previously identified the crucial role of traps in the scintillation mechanisms of small nanoscintillators. To further investigate this effect, we performed thermoluminescence experiments and radioluminescence as a function of temperature in the 10 – 320 K range on aerogels doped with 0.4% cerium and treated at 750° C under air and Ar + $H_2$ atmospheres. Because aerogels are known to act as thermal insulators, we performed the TSL measurements on gently crushed powders obtained from the aerogels. A reference single crystal was also analyzed for comparison. It was grown by the Czochralski method (by the company Crytur Ltd. in Turnov, Czech Republic). The amount of $CeO_2$ is 0.3 wt.% The details of the single crystal are reported in the following reference [45].

The single crystal exhibits the series of previously reported peaks, with the dominant peak at 95 K assigned to an antisite defect (Figure 7a) [46]. The aerogel glow curve exhibits a very weak TSL intensity, and the features appear as a broad signal detected over a temperature range that partially overlaps the ones where a series of peaks are observed in the single crystal. In particular, the glow curve of the aerogel exhibits a weak TSL peak below 50 K, superimposed on a featureless decreasing background. By comparing the TSL signal with the afterglow measured at 15 K, we can conclude that this component is thermally activated and not due to athermal tunneling effects.

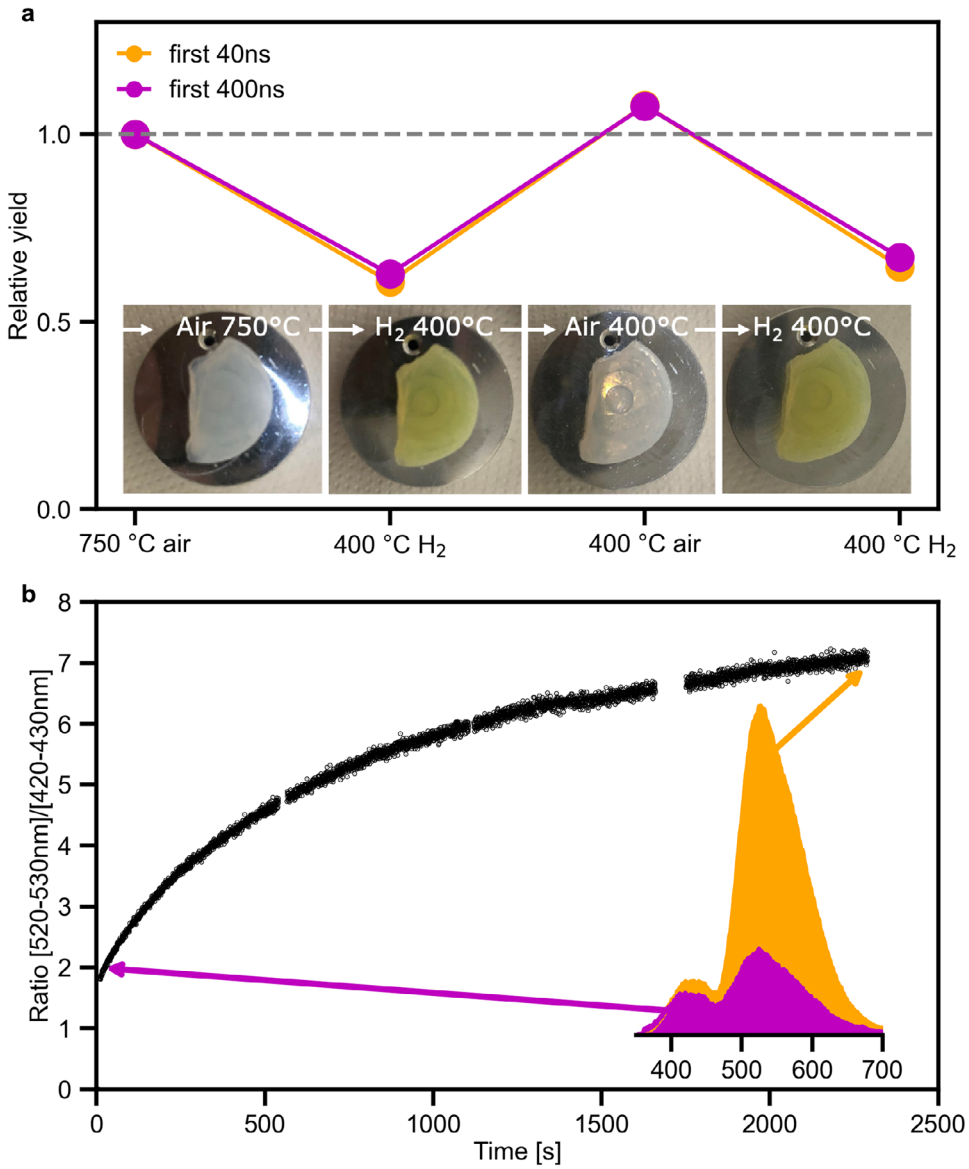


**FIGURE 8** | (a) Relative scintillation yield within 40 and 400 ns time gates after successive thermal treatments. Inset: photograph of the sample after successive thermal treatments of 1 h. (b) Variation of the photoluminescence intensity ratio (spectral area between 520–530 nm divided by the spectral area between 420–430 nm) under 355 nm laser excitation at room temperature in air.

It is important to note that, unlike the single crystal, in aerogels the $Ce^{3+}$ emission is detected neither in the TSL nor in the afterglow spectrum. In fact only a composite emission centred around 2.8 eV is observed (see Figure S8). This could possibly be due to the fact that the defect releasing charges during TSL act as hole traps. Recombination therefore cannot occur at Ce centres but rather at some luminescent point defect possibly related to surface sites, given the high surface to volume ratio of the porous aerogel structure. However, regardless of the nature of the traps, they can compete with Ce ions in charge capture during irradiation and affect the scintillation yield.

The TSL glow curves are fully consistent with the data presented in Figure 7b,c. The evolution of the scintillation intensity as a function of temperature for the single crystal shows a pronounced decrease when the temperature is lowered below 100 K, precisely where the traps become stable and begin to compete with the luminescent centres in the charge capture. In contrast, the aerogel exhibits a smooth, gradual decrease of only 10%, indicating the minor role of the involved traps at these temperatures (Figure 7b). Similarly, the evolution of the scintillation signal with irradiation time at low temperature (below the range of the TSL peaks) demonstrates a significant increase in signal intensity for the single crystal (Figure 7c). This phenomenon, known as the bright-burn effect, corresponds to the evolution of the balance between unfilled traps and the activator concentration during irradiation [47–49]. In contrast, for the YAG:Ce aerogel, we observe a slight decrease in the scintillation signal during irradiation. This decrease may be attributed to weak radiation-induced damage. Finally, when comparing the afterglow curves in Figure 7d measured at 15 K and at room temperature, one can note the pronounced delayed emission observed at temperatures below the broad series of TSL peaks, whereas the afterglow at room temperature is extremely weak (less than $10^{-5}$ of the signal

during irradiation after 1 s). All these observations indicate that the effect of traps on the dynamics of the scintillation signal in aerogels is extremely limited. The picture emerging from all these experimental data evidences, on one hand, a significant role of the thermal treatments in enhancing the luminescence yield, probably by removing non radiative recombination centers quenching Ce emission in as prepared samples. On the other hand, in the aerogels annealed at 750°C, the detrimental role of traps in scintillation is limited and significantly lower that in the SC as evidenced by the temperature dependence of the RL signal and by the bright burn profile.

### 3.5 | Reversibilty and Stability

In this final section, we address the specific sensitivity of these aerogels to the oxidation and reduction of cerium ions. In single-crystal materials, oxidation, or reduction requires prolonged thermal treatment at very high temperatures, and the resulting effect is relatively weak. As an illustration, Bok et al. [50] observed a small reduction of the $Ce^{3+}$absorption band at 450 nm, accompanied by a slight increase in absorption around 260 nm when a YAG:Ce crystal was treated at 1500°C in air for 12 h. This behavior is typical of the $Ce^{3+}$to $Ce^{4+}$conversion. For more efficient stabilization of the $Ce^{4+}$state, co-doping with divalent ions is often employed [33, 34]. In these nanocrystals, which have a diameter of about 12 nm, a significant fraction of the cerium ions are located near the surface and are therefore naturally susceptible to charge exchange. X-ray absorption near edge spectroscopy (XANES) measurements have shown that YAG:Ce nanocrystals (approximately 30 nm in diameter) naturally contain about 20% of cerium in the $Ce^{4+}$state[37]. We then explored the sensitivity and the reversibility of the cerium valence change in the nanoparticle-based aerogels.

In Figure 8a, the photograph shows the same broken bulk aerogel (original diameter 25 mm and thickness 10 mm). After a first thermal treatment at 750°C for 1 h, the sample appears fully white, as shown in Figure 1c, indicating near-complete oxidation of cerium to the $Ce^{4+}$state. Following a mild thermal treatment at 400°C for 1 h in reducing atmosphere, the sample regains its yellow color, demonstrating that a significant fraction of cerium has been reduced back to the $Ce^{3+}$state. To verify the reversibility, the same thermal treatment was applied under an air atmosphere, resulting in full recovery of the white color, and subsequently under an $Ar+H_2$ atmosphere. This complete color change in the bulk also demonstrates the percolating nature of the aerogel. With particular attention to the sample position, we analyzed the relative scintillation yield after the successive thermal treatment steps using pulsed X-ray excitation. The integrated signal over the first 40 and 400 ns appears reproducible, with a difference of approximately 40% in the case of the $Ce^{3+}$-stabilized sample. This effect demonstrates the extreme sensitivity of the aerogel to the oxidation–reduction of cerium.

One may also notice the significant difference in the observed scintillation yield between the two oxidation states. In the present measurements, we observed a 40% difference, whereas using the multi-mass sample method, we previously found a 20% difference (Figure 4b. It should be noted that in the experiments discussed here, scintillation measurements were performed immediately after the thermal treatment, while in the multi-mass sample method, measurements were carried out several weeks after sample preparation. The extreme sensitivity of the aerogels to air may lead to changes in cerium valence over time, even at room temperature; a long-term study of this effect is currently ongoing.

We also performed laser illumination at 355 nm with a power of 1 μ W (unfocused beam diameter of 2 mm) on aerogels treated in air. Since all cerium is expected to be in the $Ce^{4+}$state, no absorption bands are present except the charge-transfer bands of $Ce^{4+}$(see Figure 2b), and the PL signal from $Ce^{3+}$would therefore be expected to be absent. However, we observed a weak emission composed of a blue and a yellow band. The latter resembles the characteristic $Ce^{3+}$emission, with a slight blue shift, as observed in as-prepared or weakly annealed samples (see Figure S1). The PLE spectrum of the blue band exhibits an excitation band at 330 nm, compared to 340 nm for cerium in the 3+ oxidation state (Figure S1). It appears that during irradiation, the ratio between these two bands evolves strongly, increasingly favoring the $Ce^{3+}$emission (see Figure 8b and its inset). This behavior can reasonably be attributed to photo-reduction of cerium: under illumination, $Ce^{4+}$is partially reduced to $Ce^{3+}$, restoring the 450 nm absorption band and increasing the PL intensity. This extreme sensitivity of YAG:Ce nanoparticles to the gas environment has already been observed, and their potential use as optical pressure sensors has even been suggested [51].

## 4 | Conclusions

In this work, we have analyzed the scintillating properties of YAG:Ce aerogels. We found that the optimal cerium concentration lies between 0.1 and 0.4 wt.%. We also demonstrated that thermal treatment plays a crucial role: compared to as-prepared aerogels, samples treated at 1000°C in air show a threefold increase in scintillation yield, while the decay under X-ray excitation remains unaffected. The oxidation state of cerium also influences the light yield. Thermal treatment under a reducing atmosphere leads to a 20–40% decrease in yield, again without significantly affecting the scintillation timing properties. Importantly, cerium oxidation can be effectively controlled under relatively mild conditions (400°C for 1 h), indicating rapid gas penetration throughout the aerogel. This observation suggests that the $Ce^{3+}$/ $Ce^{4+}$ratio may evolve under room-temperature operation in air, a key consideration for the long-term functionality of detectors.

**Acknowledgements**

This research was performed in the framework of RadonNET (23IND07), funded by the European Partnership on Metrology, co-financed by the European Union's Horizon Europe Research and Innovation Programme and by the Participating States (Funder ID: 10.13039/100019599).

Open access publication funding provided by COUPERIN CY26.

**Conflicts of Interest**

The authors declare no conflicts of interest.

## Data Availability Statement

The data that support the findings of this study are available on request from the corresponding author. The data are not publicly available due to privacy or ethical restrictions.

## References


1. M. J. Weber, "Inorganic Scintillators: Today and Tomorrow," *Journal of Luminescence* 100, no. 1–4 (December 2002): 35–45, https://doi.org/10.1016/S0022-2313(02)00423-4.

2. M. Nikl and A. Yoshikawa, "Recent R&D Trends in Inorganic Single-Crystal Scintillator Materials for Radiation Detection," *Advanced Optical Materials* 3, no. 4 (April 2015): 463–481.

3. C. Dujardin, E. Auffray, E. Bourret-Courchesne, et al., "Needs, Trends, and Advances in Inorganic Scintillators," *IEEE Transactions on Nuclear Science* 65, no. 8 (August 2018): 1977–1997, https://doi.org/10.1109/TNS.2018.2840160.

4. T. Yanagida, "Inorganic Scintillating Materials and Scintillation Detectors," *Proceedings of the Japan Academy, Series B* 94, no. 2 (2018): 75–97, https://doi.org/10.2183/pjab.94.007.

5. Z. Wang, C. Dujardin, M. S. Freeman, et al., "Needs, Trends, and Advances in Scintillators for Radiographic Imaging and Tomography," *IEEE Transactions on Nuclear Science* 70, no. 7 (July 2023): 1244–1280, https://doi.org/10.1109/TNS.2023.3290826.

6. P. Dorenbos, "(Invited) The Quest for High Resolution $\gamma$-Ray Scintillators," *Optical Materials: X* 1 (January 2019): 100021, https://doi.org/10.1016/j.omx.2019.100021.

7. V. Nagarkar, T. Gupta, S. Miller, Y. Klugerman, M. Squillante, and G. Entine, "Structured Csi(tl) Scintillators for X-Ray Imaging Applications," *IEEE Transactions on Nuclear Science* 45, no. 3 (June 1998): 492–496, https://doi.org/10.1109/23.682433.

8. Y. Hormozan, I. Sychugov, and J. Linnros, "High-Resolution X-Ray Imaging Using a Structured Scintillator," *Medical Physics* 43, no. 2 (January 2016): 696–701, https://doi.org/10.1118/1.4939258.

9. A. Koch, C. Raven, P. Spanne, and A. Snigirev, "X-Ray Imaging with Submicrometer Resolution Employing Transparent Luminescent Screens," *Journal of the Optical Society of America A* 15, no. 7 (July 1998): 1940, https://doi.org/10.1364/JOSAA.15.001940.

10. T. Martin and A. Koch, "Recent Developments in X-Ray Imaging with Micrometer Spatial Resolution," *Journal of Synchrotron Radiation* 13, no. 2 (February 2006): 180–194, https://doi.org/10.1107/S0909049506000550.

11. L. Wollesen, F. Riva, P.-A. Douissard, K. Pauwels, T. Martin, and C. Dujardin, "Scintillating Thin Film Design for Ultimate High Resolution X-Ray Imaging," *Journal of Materials Chemistry C* 10, no. 24 (2022): 9257–9265, https://doi.org/10.1039/D2TC01274J.

12. P. Lecoq, "Metamaterials for Novel X- or Gamma-Ray Detector Designs," in *2008 IEEE Nuclear Science Symposium Conference Record* (IEEE, October 2008), 1405–1409, http://ieeexplore.ieee.org/document/4774678/.

13. M. Lucchini, T. Medvedeva, K. Pauwels, et al., "Test Beam Results with LuAG Fibers for Next-Generation Calorimeters," *Journal of Instrumentation* 8, no. 10 (2013): P10017, http://stacks.iop.org/1748-0221/8/i=10/a=P10017.

14. W. Chen and J. Zhang, "Using Nanoparticles to Enable Simultaneous Radiation and Photodynamic Therapies for Cancer Treatment," *Journal of Nanoscience and Nanotechnology* 6, no. 4 (April 2006): 1159–1166.

15. C. Dujardin, A.-L. Bulin, and A. Vasil'ev, "Physical Mechanisms of Deep Tissue Photodynamic Therapy Using Nanoscintillators: A Roadmap for Designing Efficient Platforms," *Journal of Luminescence* 289 (January 2026): 121570, https://doi.org/10.1016/j.jlumin.2025.121570.

16. V. Secchi, F. Cova, I. Villa, et al., "Energy Partitioning in Multicomponent Nanoscintillators for Enhanced Localized Radiotherapy," *ACS Applied Materials and Interfaces* 15, no. 20 (May 2023): 24693–24700, https://doi.org/10.1021/acsami.3c00853.

17. C. Liu, Z. Li, T. J. Hajagos, D. Kishpaugh, D. Y. Chen, and Q. Pei, "Transparent Ultra-High-Loading Quantum Dot/Polymer Nanocomposite Monolith for Gamma Scintillation," *ACS Nano* 11, no. 6 (June 2017): 6422–6430, https://doi.org/10.1021/acsnano.7b02923.

18. T. Haposan, M. Makowski, D. Kowal, et al., "The Incorporation of $CsCu_2I_3$ Nanocrystals into Polydimethylsiloxane Matrix for X- and $\gamma$-Ray Scintillators," *physica status solidi (RRL) – Rapid Research Letters* 19, no. 3 (December 2024), https://doi.org/10.1002/pssr.202400298.

19. P. Li, W. Cheng, Y. Zhou, et al., "Large Scale Bn-Perovskite Nanocomposite Aerogel Scintillator for Thermal Neutron Detection," *Advanced Materials* 35, no. 25 (April 2023), https://doi.org/10.1002/adma.202209452.

20. R. Marie-Luce, P. Mai, F. Lerouge, et al., "Real-Time Detection and Discrimination of Radioactive Gas Mixtures Using Nanoporous Inorganic Scintillators," *Nature Photonics* 18, no. 10 (September 2024): 1037–1043, https://doi.org/10.1038/s41566-024-01507-x.

21. M. Orfano, J. Perego, F. Cova, et al., "Efficient Radioactive Gas Detection by Scintillating Porous Metal–Organic Frameworks," *Nature Photonics* 17, no. 8 (2023): 672–678.

22. S. Mauree, V. Villemot, M. Hamel, et al., "Detection of Radioactive Gas with Scintillating MOFs," *Advanced Functional Materials* 2302877 (April 2023), https://doi.org/10.1002/adfm.202302877.

23. S. Senapati, V. Secchi, F. Cova, et al., "Noninvasive Treatment of Alzheimer's Disease with Scintillating Nanotubes," *Advanced Healthcare Materials* 12, no. 32 (November 2023), https://doi.org/10.1002/adhm.202301527.

24. I. Muñoz Velasco, P. Colonna, S. Sousa Nobre, et al., "Exploring the Potential of a Radioluminescent Light Source for Photobiomodulation," *IEEE Transactions on Nuclear Science* 72, no. 7 (July 2025): 2089–2096, https://doi.org/10.1109/TNS.2025.3541916.

25. M. A. Prelas, C. L. Weaver, M. L. Watermann, E. D. Lukosi, R. J. Schott, and D. A. Wisniewski, "A Review of Nuclear Batteries," *Progress in Nuclear Energy* 75 (August 2014): 117–148.

26. M. G. Spencer and T. Alam, "High Power Direct Energy Conversion by Nuclear Batteries," *Applied Physics Reviews* 6, no. 3 (September 2019): 031305.

27. M. Odziomek, F. Chaput, F. Lerouge, M. Sitarz, and S. Parola, "Highly Luminescent YAG:Ce Ultra-Small Nanocrystals, from Stable Dispersions to Thin Films," *Journal of Materials Chemistry C* 5 (2017): 12 561–12 570.

28. R. Broda, P. Cassette, and K. Kossert, "Radionuclide Metrology Using Liquid Scintillation Counting," *Metrologia* 44, no. 4 (2007): S36.

29. B. Sabot, C. Dutsov, P. Cassette, et al., "A Compact Detector System for Simultaneous Measurements of the Light Yield Non-Linearity and Timing Properties of Scintillators," *Scientific Reports* 14, no. 1 (2024): 6960.

30. M. J. Odziomek, "Colloidal Synthesis and Controlled 2D/3D Assemblies of Oxide Nanoparticles," Thèses, Université de Lyon; AGH University of Science and Technology (Cracovie, Pologne), (December 2017), https://theses.hal.science/tel-01968032.

31. R. Kasuya, T. Isobe, H. Kuma, and J. Katano, "Photoluminescence Enhancement of Peg-Modified YAG:$Ce^{3+}$ Nanocrystal Phosphor Prepared by Glycothermal Method," *The Journal of Physical Chemistry B* 109, no. 47 (November 2005): 22126–22130, https://doi.org/10.1021/jp052753j.

32. M. Nyman, L. E. Shea-Rohwer, J. E. Martin, and P. Provencio, "Nano-YAG:Ce Mechanisms of Growth and Epoxy-Encapsulation," *Chemistry of Materials* 21, no. 8 (April 2009): 1536–1542, https://doi.org/10.1021/cm803137h.

33. S. Blahuta, A. Bessiere, B. Viana, P. Dorenbos, and V. Ouspenski, "Evidence and Consequences of $Ce^{4+}$ in LYSO:Ce,Ca and LYSO:Ce,Mg Single Crystals for Medical Imaging Applications," *IEEE Transactions on Nuclear Science* 60, no. 4 (, August 2013): 3134–3141.

34. M. Nikl, K. Kamada, V. Babin, et al., "Defect Engineering in Ce-Doped Aluminum Garnet Single Crystal Scintillators," *Crystal Growth & Design* 14, no. 9 (August 2014): 4827–4833.

35. F. Moretti, A. Vedda, N. Chiodini, et al., "Incorporation of $Ce^{3+}$ in Crystalline Gd-Silicate Nanoclusters Formed in Silica," *Journal of Luminescence* 132, no. 2 (February 2012): 461–466, https://doi.org/10.1016/j.jlumin.2011.09.016.

36. V. Bachmann, C. Ronda, and A. Meijerink, "Temperature Quenching of Yellow $Ce^{3+}$ Luminescence in YAG:Ce," *Chemistry of Materials* 21, no. 10 (May 2009): 2077–2084, https://doi.org/10.1021/cm8030768.

37. A. Cantarano, D. Testemale, E. Homeyer, et al., "Drastic $Ce^{3+}$ Insertion Enhancement in Yag Garnet Nanocrystals through a Solvothermal Route," *Frontiers in Materials* 8 (November 2021), https://doi.org/10.3389/fmats.2021.768087.

38. V. LeBihan, A. Pillonnet, D. Amans, G. Ledoux, O. Marty, and C. Dujardin, "Critical Dimension Where the Macroscopic Definition of Refractive Index Can Be Applied at a Nanometric Scale," *Physical Review B* 78, no. 11 (September 2008): 113405.

39. A. Aubret, A. Pillonnet, J. Houel, C. Dujardin, and F. Kulzer, "CdSe/ZnS Quantum Dots as Sensors for the Local Refractive Index," *Nanoscale* 8, no. 4 (2016): 2317–2325, https://doi.org/10.1039/C5NR06998J.

40. R. S. Meltzer, S. P. Feofilov, B. Tissue, and H. B. Yuan, "Dependence of Fluorescence Lifetimes of $Y_2O_3$:$Eu^{3+}$ Nanoparticles on the Surrounding Medium," *Physical Review B* 60 (November 1999): R14 012–R14 015.

41. J. Bárta, V. Čuba, M. Pospíšil, V. Jarý, and M. Nikl, "Radiation-Induced Preparation of Pure and Ce-Doped Lutetium Aluminium Garnet and Its Luminescent Properties," *Journal of Materials Chemistry* 22, no. 32 (2012): 16590.

42. A. Huang, K. K. Pukhov, K.-L. Wong, and P. A. Tanner, "Temperature Dependence of the Local Field Effect in YAG:$Ce^{3+}$ Nanocomposites," *Nanoscale* 13, no. 22 (2021): 10002–10009, https://doi.org/10.1039/D1NR01469B.

43. Y.-C. Lin, M. Bettinelli, S. K. Sharma, B. Redlich, A. Speghini, and M. Karlsson, "Unraveling the Impact of Different Thermal Quenching Routes on the Luminescence Efficiency of the $Y_3Al_5O_{12}$:$Ce^{3+}$ Phosphor for White Light Emitting Diodes," *Journal of Materials Chemistry C* 8, no. 40 (2020): 14015–14027, https://doi.org/10.1039/d0tc03821k.

44. P. Ganigal, D. Van der Heggen, P. F. Smet, et al., "Uv-a Scintillation and Persistent Luminescence from Ce- and Ce/Ho-Doped $YPO_4$ Nanoparticles," *Physical Chemistry Chemical Physics* 27, no. 46 (2025): 25098–25109, https://doi.org/10.1039/D5CP02667A.

45. J. A. Mares, A. Beitlerova, M. Nikl, et al., "Time Development of Scintillating Response in Ce- or Pr-Doped Crystals," *physica status solidi c* 4, no. 3 (March 2007): 996–999, https://doi.org/10.1002/pssc.200673858.

46. E. Mihóková, M. Nikl, J. Mareš, et al., "Luminescence and Scintillation Properties of YAG:Ce Single Crystal and Optical Ceramics," *Journal of Luminescence* 126, no. 1 (September 2007): 77–80, https://doi.org/10.1016/j.jlumin.2006.05.004.

47. M. Fasoli, N. Chiodini, A. Lauria, F. Moretti, and A. Vedda, "Effect of Deep Traps on the Optical Properties of $Tb^{3+}$ Doped Sol-Gel Silica," *physica status solidi c* 4, no. 3 (March 2007): 1056–1059, https://doi.org/10.1002/pssc.200673880.

48. F. Moretti, G. Patton, A. Belsky, et al., "Radioluminescence Sensitization in Scintillators and Phosphors: Trap Engineering and Modeling," *The Journal of Physical Chemistry C* 118, no. 18 (April 2014): 9670–9676, https://doi.org/10.1021/jp501717z.

49. F. Cova, M. Girola, M. Stabile, et al., "Effect of Point Defects on the Performances of $Li_2MoO_4$ and $Li_2WO_4$ Crystals as Scintillating Cryogenic Calorimeters," *Journal of Alloys and Compounds* 1022 (April 2025): 179848, https://doi.org/10.1016/j.jallcom.2025.179848.

50. J. Bok, P. Horodyský, and V. Krzyžánek, "Effect of Oxidation Annealing on Optical Properties of Yag:Ce Single Crystals," *Optical Materials* 46 (August 2015): 591–595, https://doi.org/10.1016/j.optmat.2015.05.035.

51. S. P. Feofilov, D. V. Arsentyev, A. B. Kulinkin, et al., "Gaseous Environment-Sensitive Fluorescence of YAG:$Ce^{3+}$ Nanocrystals," *Journal of Applied Physics* 107, no. 6 (March 2010), https://doi.org/10.1063/1.3327449.

## Supporting Information

Additional supporting information can be found online in the Supporting Information section.

**Supporting File:** adom71263-sup-0001-SuppMat.pdf.